CELLULAR NEUROSCIENCE

Trans-synaptic assemblies link synaptic vesicles and neuroreceptors

Antonio Martinez-Sanchez[1,2,3,4,5], Ulrike Laugks[1]*, Zdravko Kochovski[1†], Christos Papantoniou[1], Luca Zinzula[1], Wolfgang Baumeister[1], Vladan Lučić[1‡]

Synaptic transmission is characterized by fast, tightly coupled processes and complex signaling pathways that require a precise protein organization, such as the previously reported nanodomain colocalization of pre- and postsynaptic proteins. Here, we used cryo–electron tomography to visualize synaptic complexes together with their native environment comprising interacting proteins and lipids on a 2- to 4-nm scale. Using template-free detection and classification, we showed that tripartite trans-synaptic assemblies (subcolumns) link synaptic vesicles to postsynaptic receptors and established that a particular displacement between directly interacting complexes characterizes subcolumns. Furthermore, we obtained de novo average structures of ionotropic glutamate receptors in their physiological composition, embedded in plasma membrane. These data support the hypothesis that synaptic function is carried by precisely organized trans-synaptic units. It provides a framework for further exploration of synaptic and other large molecular assemblies that link different cells or cellular regions and may require weak or transient interactions to exert their function.

INTRODUCTION

Most cellular processes are carried out by molecular assemblies that form functional modules and require a distinctly nonrandom spatial organization of their components (*1*, *2*). Several postsynaptic, presynaptic, and cell-adhesion proteins, as well as neurotransmitter release sites are organized in nanoscale domains (*3*–*10*). The importance of these nanodomains is exemplified by the findings that diffusion of α-amino-3-hydroxy-5-methyl-4-isoxazole propionic acid receptors (AMPARs) along the postsynaptic membrane of glutamatergic synapses can be arrested within specific nanodomains (*5*, *6*) and is required for mechanisms underlying higher cognitive processes (*11*). Furthermore, evidence is accumulating that the response at glutamatergic synapses depends on the exact positioning of postsynaptic receptors in respect to presynaptic release complexes and that colocalization of nanodomains forms functional assemblies that may control synaptic strength (*12*). The finding that nanodomains containing some of the pre- and postsynaptic proteins directly involved in synaptic transmission colocalize across the synaptic cleft to form trans-synaptic nanoassemblies (termed synaptic nanocolumns) was a crucial step in that direction (*4*). While these observations, obtained by superresolution fluorescence microscopy, reach a precision of few tens of nanometers, direct observation of these nanoassemblies is currently lacking. Furthermore, many fundamental aspects of trans-synaptic nanoassemblies are still unresolved, such as the mechanism responsible for the trans-synaptic alignment and the existence of basic discrete units within nanocolumns.

Ionotropic glutamate receptors (iGluRs) mediate synaptic transmission at excitatory synapses (*13*). Among them, AMPAR and *N*-methyl-D-aspartate receptors (NMDARs) are prominent components of synaptic nanodomains and are essential for long-term potentiation (*14*). They are composed of four pore-forming subunits but may contain several auxiliary subunits and form larger complexes (*2*, *15*). While a recent series of high-resolution structures of AMPARs and NMDARs provided important information about their function, these structures were obtained from reconstituted receptors that were altered in different ways to improve their expression and stability (*16*–*19*) and/or removed from their native lipids by detergent extraction (*20*). Therefore, there is a need to obtain structures of AMPAR and NMDAR in their native physiological conformations, subunit composition, and lipid environment.

Cryo–electron tomography (cryo-ET) is uniquely suited for the comprehensive, three-dimensional (3D) imaging of molecular complexes in their native context at the molecular resolution (*21*). Cellular samples are rapidly frozen and imaged in the same vitrified, fully hydrated state (*22*, *23*). This is in contrast to procedures that use chemical fixation, dehydration, and heavy-metal staining, which, although essential for our current understanding of cellular ultrastructure, are known to induce membrane deformation, rearrangements, and aggregation of cytosolic material, thus obscuring fine biological structures and precluding molecular interpretation (*24*–*27*).

To overcome problems arising from the presence of many molecular species and molecular crowding, here we extended the procedure we recently developed for automated, template-free detection and unsupervised classification of heterogeneous membrane-bound complexes (fig. S1) (*28*). This allowed us to localize different synaptic complexes at a single-nanometer precision, obtain their native average structures, explore their relation to synaptic vesicles (SVs) and synaptic plasma membranes, and resolve the trans-synaptic assemblies that they form.

RESULTS

Validation of the synaptosomal preparation

Synaptosomes are a well-established model for neurotransmitter release and are susceptible to pharmacological manipulations (*29*, *30*). Previously,

[1]Max Planck Institute of Biochemistry, Am Klopferspitz 18, 82152 Martinsried, Germany. [2]Department of Computer Sciences, Faculty of Sciences, University of Oviedo, Federico Garcia Lorca 18, 33007, Spain. [3]Instituto de Investigación Sanitaria del Principado de Asturias, University of Oviedo, Avenida Hospital Universitario s/n, 33011 Oviedo, Spain. [4]Institute of Neuropathology, University Medical Center Göttingen, 37075 Göttingen, Germany. [5]Cluster of Excellence "Multiscale Bioimaging: from Molecular Machines to Networks of Excitable Cells" (MBExC), University of Göttingen, Göttingen, Germany.
*Present address: Centre for Structural Systems Biology (CSSB), Heinrich Pette Institut, Leibniz-Institut für Experimentelle Virologie, DESY Building 15, Notkestr. 85, 22607 Hamburg, Germany.
†Present address: Institute of Electrochemical Energy Storage, Helmholtz-Zentrum Berlin für Materialien und Energie, 14109 Berlin, Germany.
‡Corresponding author. Email: vladan@biochem.mpg.de

other laboratories showed and we confirmed that synaptosomes are capable of multiple rounds of Ca^{2+}- dependent neurotransmitter release (*31*–*33*). The Percoll-based synaptosomal preparation that we used is considered to be superior to other preparations because it maintains osmolarity and requires a shorter centrifugation time (*30*). Synaptosomes prepared in this way were found to respond to a range of pharmacological treatments in biochemical assays and by structural observations and structural analysis (*32*–*34*).

To activate postsynaptic NMDAR-type glutamate receptors and cause Ca^{2+} influx, we stimulated synaptosomes with the NMDAR agonist glutamate and the co-agonist glycine, with and without KCl, and isolated the postsynaptic density (PSD) fraction from the stimulated and nonstimulated (control) synaptosomes. We observed a significant stimulation-dependent increase of total (*t* test, $P = 0.057$ without KCl and $P = 0.00012$ with KCl, $N = 8$) and T286-phosphorylated calcium/calmodulin-dependent protein kinase IIα (CaMKIIα) in the PSD fraction (fig. S2A) (*t* test, $P = 0.0085$ without KCl and $P = 0.0056$ with KCl). Considering the postsynaptic localization of NMDARs and a large postsynaptic presence of CaMKII, our results show that upon stimulation, likely due to Ca^{2+} influx, postsynaptic CaMKII was activated, autophosphorylated, and inserted into the core of the PSD that comprises the PSD fraction. This is similar to the previously shown NMDAR stimulation-dependent CaMKII translocation to the PSD in neuronal cultures (*35*). Therefore, our data strongly argue that postsynaptic parts of synaptosomes respond to stimulation by neurotransmitters.

As another method to access the integrity of our synaptosomal fractions, we used tandem mass spectrometry (MS) to determine the relative molar amounts of proteins present in the starting material (neocortical homogenate), an intermediate fraction (crude synaptosomal fraction or P2), and the final (Percoll-based) synaptosomes. Ranking of prominent pre- and postsynaptic proteins showed that their relative importance increased during the preparation, indicating that synapses were purified by the fractionation (fig. S2B). Next, we selected more than 100 synaptic proteins and determined the molar amount ratios between the selected and the reference protein (Bassoon for presynaptic and PSD-95 for postsynaptic). Most of the ratios obtained for the synaptosomes were similar to those from the homogenate (fig. S2C), indicating that the relative abundance of synaptic proteins was, to a large extent, maintained during the preparation. Last, we showed that our data are consistent with previous quantifications, by comparing the selected presynaptic proteins with the absolute values (*36*) and the selected postsynaptic proteins with the existing absolute quantifications obtained by fluorescence and immunolabeling (*37*, *38*) and with relative (MS) data (fig. S2D) (*36*, *39*). In addition, our data provide stoichiometry of several proteins not covered in the studies mentioned above. Together, our data show that, to a large extent, our synaptosomal preparation preserves the protein composition of the synapse.

Detection of synaptic complexes in cryo-tomograms

Cryo–electron tomograms of rodent neocortical synaptosomes analyzed in this study showed smooth, continuous membranes, nonaggregated cytosolic material, and well-resolved intra- and extracellular complexes, in agreement with previous cryo-ET investigations of synaptosomes and neuronal cultures (*26*, *33*, *40*–*43*).

Cryo-ET density was traced in 3D using the discrete Morse theory segmentation and the topological persistence simplification (see Materials and Methods) (*28*, *44*). The resulting network of grayscale minima, saddle points, and arcs provided an accurate representation of the proteins and lipids present at the synapse (Fig. 1, A and B, and movie S1). By imposing geometrical constraints on the detected density, we detected membrane-bound complexes located at different synaptic layers: SV tethers (presynaptic cytosolic layer) and extracellular presynaptic, extracellular postsynaptic, and intracellular postsynaptic complexes (Fig. 1C). We also determined centroids of spatial clusters of tethers. In this way, density tracing and detection of complexes (together comprising particle picking) yield particle sets where template-based picking bias is avoided.

Classification of synaptic complexes

The particle sets obtained comprise different types of synaptic membrane-attached complexes, which reflect the inherent variability of molecular compositions and conformational states. The number and abundance of structurally similar types of complexes present at the synapse are not known a priori. We used the affinity propagation (AP) clustering to classify the particle sets according to their morphological features and remove false-positive complexes, because AP is better suited for this task than the other commonly used methods (*28*, *45*). As rotational averages around vectors normal to the plasma membrane were subjected to AP clustering, the results were sensitive to the particle orientation with respect to the membrane, but not to the rotation around the membrane normal.

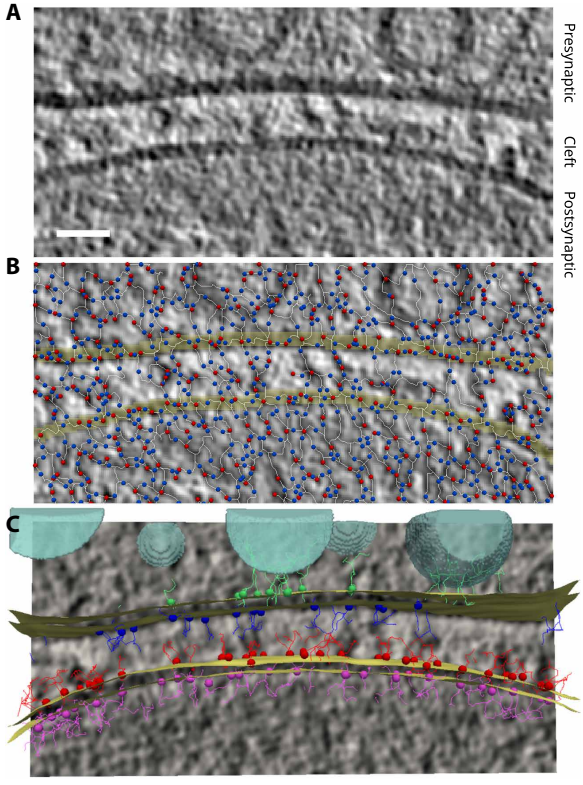

Fig. 1. Detecting synaptic complexes. (**A**) Tomographic slice, 0.68 nm in thickness. (**B**) Tracing density using the procedure based on the discrete Morse theory. Red circles represent grayscale minima (graph vertices), the blue ones are the saddle points, and the white lines are arcs. Only for this panel that the tracing was done on a single tomographic slice in 2D; all other processing was performed on tomograms, in 3D. (**C**) Detected particles: tethers (green), extracellular presynaptic (blue), extracellular postsynaptic (red), and intracellular postsynaptic (pink). SVs are shown in turquoise, and plasma membranes are shown in yellow. Scale bar, 20 nm.

The first AP classification served to select extracellular particles that showed clear membrane-bound densities, yielding pre AP1 and post AP1 particle sets (fig. S3, A and C). The discarded classes likely contained complexes that had weak or flexible membrane attachment domains, as well as classes composed of a mixture of heterogeneous complexes. In the second AP classification round, classes lacking a well-resolved extracellular density were discarded, yielding pre and post AP2 sets (fig. S3, B and D). The remaining classes were merged on the basis of visual similarity into four presynaptic (pre AP2p-s) and four postsynaptic classes (post AP2a, AP2b, AP2c, and AP2n), and their de novo (external reference-free) 3D averages were determined (Fig. 2, A and B).

On the basis of the abundance of synaptic adhesion proteins (fig. S2D), we can speculate that SynCAMs and neurexins are prominent in some of the presynaptic classes. Complexes present in low-copy numbers were likely discarded during the AP classification because their number was insufficient to produce well-resolved averages or attributed to the more heterogeneous classes. For example, in an unlikely case that despite our selection procedure an inhibitory synapse was analyzed, these receptors would most likely be classified in one of the most heterogeneous classes (post AP2b or AP2c) or removed during the AP classification because of the size difference between iGluRs and $GABA_A$ (γ-aminobutyric acid type A) receptors (fig. S4C) and the small number of $GABA_A$ receptors that would be included in our particle set. Therefore, we conclude that the average structures we obtained most likely represent distinct groups of pre- and postsynaptic complexes.

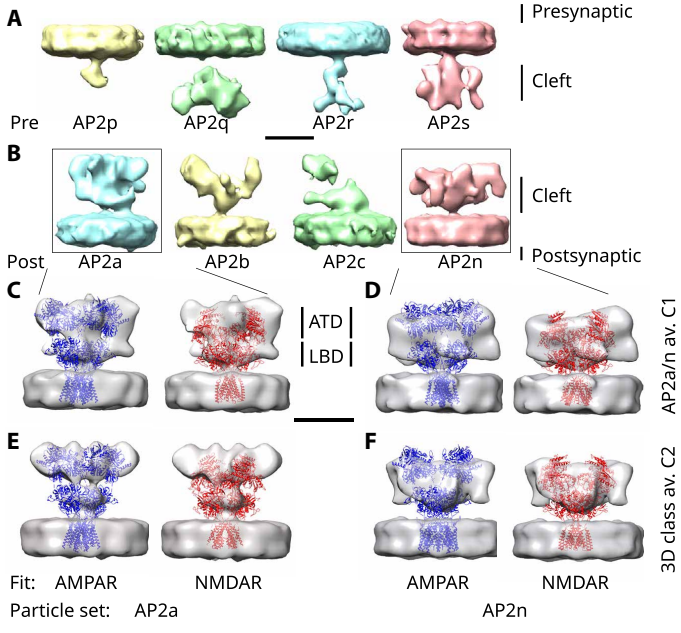

Fig. 2. De novo average densities of extracellular presynaptic complexes. (**A**) Presynaptic AP2 class averages, from left to right AP2p-s. (**B**) Postsynaptic AP2 class averages, from left to right AP2a, AP2b, AP2c, and AP2n. There is no color coding in (A) and (B); different colors are used only to distinguish the densities. (**C**) Postsynaptic AP2a class average. (**D**) Postsynaptic AP2n class average. (**E**) 3D class average with C2 symmetry derived from AP2a. (**F**) 3D class average with C2 symmetry derived from AP2n. (C to F) In each case, the same density (gray) is shown twice: on the left atomic model of AMPAR (blue, PDB-6QKZ) is fitted in the density and on the right NMDAR model (red, PDB-6MMP). Scale bars, 10 nm.

Our de novo class averages showed complexes of various size and distinct morphology (Fig. 2, A and B). Postsynaptic AP class averages were larger in size and had different shapes than the presynaptic ones, although the identical procedure was applied to pre- and postsynaptic sides, confirming the resolving power of our detection and classification procedure. Furthermore, we applied the same density tracing, particle picking, and AP classification procedure on the extracellular side of perisynaptic membrane of the postsynaptic terminals. The AP1 classification did not yield any class that would be accepted for further processing according to criteria we used for synaptic complexes (fig. S3E). Nevertheless, we subjected all particles to the next step in our procedure, the second round of AP classification. As expected, this did not result in averages comparable to the synaptic post AP2 classes (fig. S3, D and F). Together, these results show that perisynaptic complexes are much smaller or present at a much lower density than the synaptic complexes and thus confirm the specific postsynaptic localization of the post AP2a and AP2n particles.

Structure determination of iGluRs

Among the four postsynaptic classes, the average AP2a and AP2n densities were well resolved (Fig. 2B). Subsequent de novo 3D classification of AP2a and AP2n sets obtained (fig. S1) without and with C2 symmetry (fig. S7, A and B) yielded better resolved averages (fig. S4D and Fig. 2, E and F).

Several lines of evidence argue that iGluRs are the major constituents of AP2a and AP2n sets. (i) The overall size of the extracellular region of all AP2a and AP2n averages (maximal height and width > 10 nm) matched that of the available iGluR structures. (ii) This size was much larger than the extracellular region of all currently available structures of membrane-bound postsynaptic and synaptic adhesion proteins/complexes, except for other iGluRs (Fig. 2, C to F, and fig. S4, A to C) (*46*, *47*). (iii) Other large complexes, such as the voltage-gated Na, Ca, and K channels, do not have extracellular amino acid sequences that are long enough to match that of iGluRs (approximately 340 kDa). (iv) Applications of the same procedure on the presynaptic membrane and on the perisynaptic part of the postsynaptic membrane did not yield averages of size similar to post AP2a and AP2n averages. (v) Our averages showed the main morphological features of iGluRs, the membrane-proximal ligand-binding domains (LBDs) and membrane-distal amino-terminal domains (ATDs) (Fig. 2, C and F). The averages had an approximate twofold symmetry around the axis perpendicular to the membrane, consistent with the architecture of iGluRs composed of four pore-forming subunits with their ATDs and LBDs organized as dimer-of-dimers. Together, our data argue that iGluRs are the major constituents of AP2a and AP2n sets.

It was previously determined that pore-forming subunits of AMPAR and NMDAR-type iGluRs (GluA1, GluA2, GluN1, and GluN2) are among the most highly expressed postsynaptic membrane-bound proteins (*48*). Other iGluR types, kainate and delta receptors, are not expected to be prominent on the postsynaptic side of neocortical synapses (*49*, *50*). Our MS data confirmed these results (fig. S2D): The protein copy numbers per synapse were 333 ± 57 (mean ± SD) for AMPAR subunits (GluA1 and GluA2), 121 ± 32 for NMDAR subunits (GluN1, GluN2A, and GluN2B), 17 ± 4.9 for kinate subunits (GluK2, GluK3, and GluK5), and 4.6 ± 1.2 for delta receptor subunits (GluD1). These strongly argue that AMPARs and NMDARs are the major components of AP2a and AP2n sets.

The mean number of AP2a and AP2n particles per synapse was 40 and 38, respectively. The number of AMPARs and NMDARs in the postsynaptic fraction was estimated to be 15 and 20, which is most likely an underestimate for the number of these receptors at the synapse because of the detergent-based extraction procedure (*48*). The summation of all AMPAR and NMDAR subunits in our MS data (fig. S2D) results in 83 (tetrameric) AMPARs and 30 NMDARs.

Despite their overall similarity, post AP2a and AP2n class averages had a sufficient level of detail to allow us to detect important differences between them. The AP2a class average was taller than the AP2n, consistent with the difference between AMPAR and NMDAR-type iGluRs (Fig. 2, C and D, and figs. S4, A and B, S5A, and S6A). Furthermore, the AP2a average adopted a "Y shape," with open membrane-distal regions, characteristic of AMPARs and showed further separated LBD and ATD domains (*16*). The AP2n average had a more compact form, where the lower, membrane-proximal region was more prominent, making it similar to NMDARs (*51*). Therefore, AP2a and AP2n classes likely represent AMPARs and NMDARs, respectively.

Next, we fit the following three iGluR atomic models in all our de novo averages: a very recent atomic model of AMPAR that has the closest to physiological subunit composition obtained so far and two recent NMDAR models that represent the array of conformational states of NMDAR (figs. S5, A to C, and S6, A to C) (*16*, *18*). The height and the shape of de novo averages derived from the AP2a matched better AMPAR, while those derived from AP2n particle matched better NMDAR models.

Proceeding with the atomic initial model–based 3D classification and refinement of putative AMPAR (AP2a) and NMDAR (AP2n) particles (figs. S1 and S7, C and D), we obtained averages that were consistent with known structures (figs. S5D and S6, D and E). The observation that two high-resolution structures of NMDAR representing different conformations match different parts of the average densities obtained from post AP2n particle sets (fig. S6) indicates that this set likely contains receptors in different conformations that reflect different physiological states. When the initial models were exchanged, 3D classification of each set converged to averages similar to those obtained from the same particle set and not to the exchanged initial models (fig. S8), thus further supporting the molecular assignment of AP2a and AP2n sets. Together, the data presented strongly argue that our average densities show iGluRs and that the AP2a class is dominated by AMPARs and the AP2n by NMDARs.

We also obtained average densities from an additional, completely independent particle set. Synaptosomes were isolated using the same protocol, and the processing followed the same procedure used above. Although this set was poorer in quality than the post AP2a and AP2n sets (larger pixel size and overall lower contrast), the averages obtained had the same size and overall shape as those derived from post AP2a and AP2n sets (fig. S8, C and D). This provides an independent confirmation of the results obtained from the post AP2a and AP2n sets.

There were also differences between the de novo averages and the corresponding models. Extra density protruding away from the ATD of AP2a-derived averages may be caused by binding of other proteins, because other secreted and transmembrane proteins are known to bind AMPAR (*15*, *52*) and N-terminal interactions were shown to be critical for AMPAR anchoring at the synapse (*53*, *54*). Depending on the NMDAR atomic model used, extra ATD density was found toward the periphery or close to the central region (fig. S6). This argues that multiple conformations of NMDAR are present, consistent with previous structural studies showing a substantial conformational variability of NMDARs depending on subunit composition, physiological state, and buffer conditions. In addition, LBD domains were positioned further away from the membrane in our averages. This may mean that imaging using Volta phase plate negatively affected fitting or that detergents used to stabilize the transmembrane domain in single-particle electron microscopy (EM) studies did not fully substitute for native lipids.

Except for early work on negatively stained samples (*55*), all previously reported AMPAR and NMDAR structures were obtained from reconstituted or detergent-extracted receptors that, in most cases, had a nonnative pore-forming and auxiliary subunit composition (*16*–*19*). Receptors were detergent-extracted, genetically modified, and artificially stabilized, leading to high-resolution structures and the determination of atomic models, but leaving the question open to which extent they correspond to native iGluRs. This is in contrast with our samples, where iGluRs have physiological subunit compositions and are kept in their native lipid membranes together with more than 30 known auxiliary subunits and binding partners (*52*). Therefore, interactions between auxiliary and pore-forming subunits, as well as between ATD domain and other synaptic proteins (*53*, *56*), whether they are stable, transient, or dependent on the receptor state, could likely explain extra densities observed in our averages.

Trans-synaptic colocalization and subcolumns

To investigate the trans-synaptic organization of complexes, we determined the number of colocalization events between two types of complexes residing on different synaptic layers (termed 2-colocalizations, see Materials and Methods). Specifically, 2-colocalizations between pre and post AP1 and between pre and post AP2 sets showed the highest significance among all possible 2-colocalizations involving pre and post AP1 and AP2 complexes, tether centroids, and SVs (fig. S9A); relevant particle sets are indicated on the processing scheme (fig. S1). These were significant at colocalization distances (in cis-cleft directions) at 5, 10, and 15 nm, while all other 2-colocalizations showed significance in a few cases. In addition, 2-colocalizations involving tethers were generally better than the corresponding ones involving SVs.

To explore the hypothesis that larger complexes link pre- and postsynaptic terminals, we proceeded to detect 3-colocalizations, which are simultaneous trans-synaptic colocalization between complexes present on all three synaptic layers. Significant 3-colocalizations were obtained between tether centroids, pre AP1 and post AP1 complexes at 5, 10, and 15 nm and between tether centroids and the pre and post AP2 complexes at 5 and 15 nm (Fig. 3A). In contrast, although the number of tether centroids and SVs was similar and their locations were correlated, SV 3-colocalizations with AP1 complexes were significant at 10 and 25 nm, while those with AP2 complexes failed to reach significance.

The following observations argue that 15-nm colocalization distance is the most representative of the trans-synaptic organization. The number of the tether-based 3-colocalization events normalized to the colocalization area had a maximum at 15 nm (fig. S9B). The colocalization area at 5-nm distance (78.5 nm^2) is similar to the area of one AMPAR or NMDAR projected on the membrane and is thus too small to accommodate multiple complexes similar in size to iGluR's within a single 3-colocalization event. In addition, the number of 3-colocalization events at 5 nm was too small to support trans-synaptic

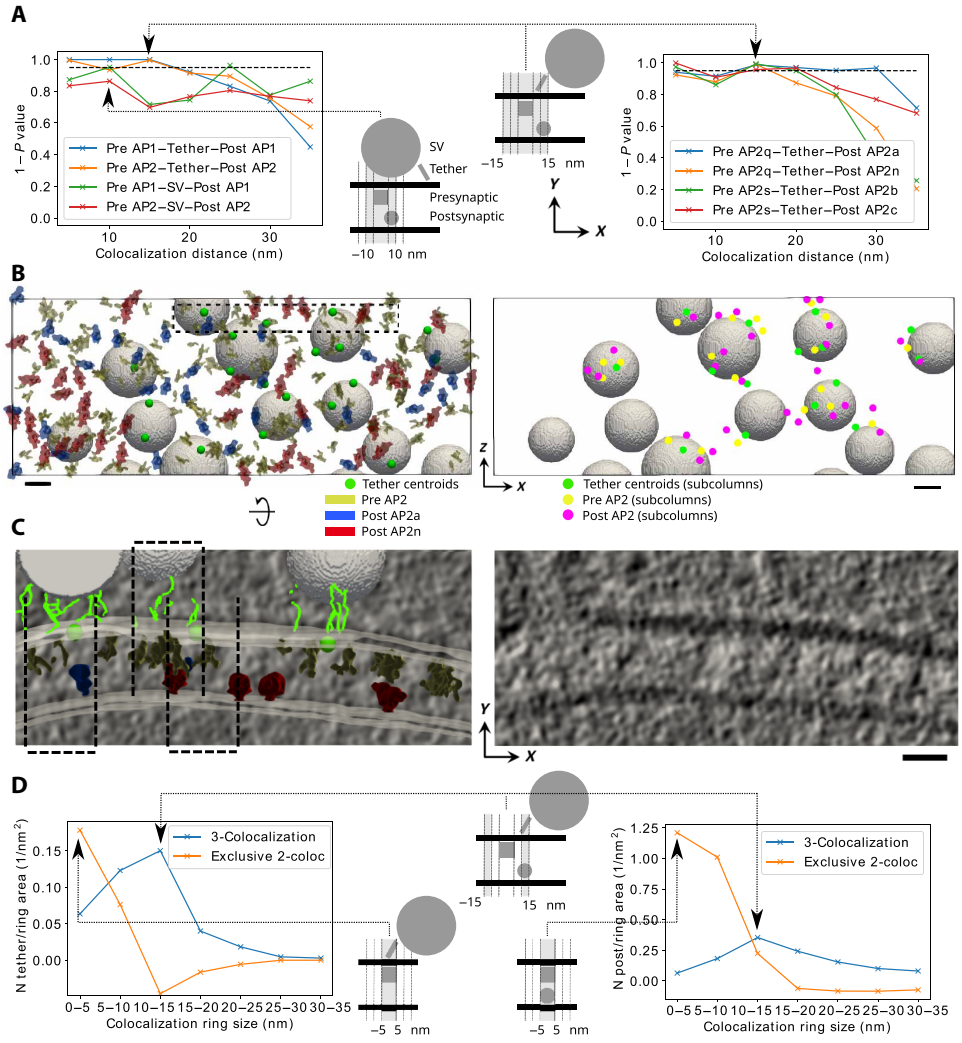

Fig. 3. Trans-synaptic colocalization. (**A**) Significance of 3-colocalizations between the indicated pre- and postsynaptic complexes and tether centroids or SVs. (**B**) View of a synapse from the postsynaptic side, where all (left) and subcolumn particles (right) are mapped at their precise locations: tether centroids (green circles), pre AP2 (yellow shapes, left, and yellow circles, right), post AP2a (blue, left), post AP2n (red, left), and all post AP2 (violet, right). (**C**) Tomographic slices corresponding to the inset shown in (B, left), viewed from the side of the synapse, with (left) and without (right) superimposed particles [green lines represent tethers, and other symbols are the same as in (B)]. Dashed rectangles show subcolums. *Y* axes show the trans-synaptic direction. (**D**) Number of tether centroids (left) and post AP2 complexes (right) in trans-synaptic rings for 3-colocalizations between tether centroids, pre AP2 and post AP2 particles (blue), and exclusive 2-colocalizations between tether centroids and pre AP2 (orange, left), and between pre and post AP2 (orange right). The data are normalized to the ring area. (A and D) Schemes in the middle illustrate single colocalization events corresponding to the most prominent data points (indicated by arrows). The shaded areas represent trans-synaptic colocalization neighborhoods (A) and rings (D). Scale bars, 20 nm.

organization. Given the significance of these events, they may form transient interactions. In addition, because the AP2 particle sets provide the most refined representation of the full complement of pre- and postsynaptic extracellular complexes, we will refer to the 3-colocalization events between tether centroids, pre AP2 and post AP2 complexes at 15 nm as subcolumns.

Therefore, our data strongly suggest that the tripartite trans-synaptic assemblies comprising tethers, pre- and postsynaptic complexes, and subcolumns, in particular, provide structural links between SVs and postsynaptic complexes and constitute a robust support for the trans-synaptic organization.

Internal subcolumn organization

To investigate the composition of subcolumns, we focused on subsets of subcolumns formed by different pre and post AP2 classes (fig. S1). Significant results were found for 3-colocalizations at 15 nm in the following combinations: pre AP2q–post AP2a, pre AP2q–post AP2n, pre AP2s–post AP2b, and pre AP2s–post AP2c (Fig. 3A and fig. S9C). This means that among presynaptic classes, AP2q and AP2s show colocalization significance, as opposed to AP2p and AP2r. The same pattern, where AP2q and AP2s show significance, as opposed to AP2p and AP2r, was observed at 2-colocalizations between tether centroids and the pre AP2 classes (fig. S9D). Furthermore, there were clear differences between pre AP2q and -AP2s complexes. 2-colocalizations tether–pre AP2s was significant for a wide range of distances, unlike tether–pre AP2q, while pre AP2q was more prominent in 3-colocalizations with iGluRs (post AP2a and AP2n) than pre AP2s. Regarding the postsynaptic classes, 34% of all AP2a particles and 29% of all AP2n particles were present in the above 3-colocalizations formed by different pre and post AP2 classes.

Together, these results show that subcolumns differ in their composition, pre AP2 classes play different roles in the trans-synaptic organization, and iGluRs are prominent in subcolumns.

Next, we proceeded to decipher the relative particle localization within subcolumns. We approached this question by determining the number of particles present within concentric cylindrical trans-synaptic rings (see the methods and the schemes in Fig. 3D and fig. S10C). The particle number (normalized to the ring area) within ring 3-colocalizations was the highest in the ring at 10 to 15 nm for both postsynaptic complexes and tether centroids (Fig. 3D). On the contrary, most of the tether centroids and postsynaptic complexes present exclusively in ring 2-colocalizations (that is, in ring 2-colocalizations, but not ring 3-colocalizations) were located in the 0- to 5-nm ring, which is strongly aligned with the presynaptic complexes. Tether centroids were essentially absent from the exclusive ring 2-colocalization at 10 to 15 nm, while the number of postsynaptic complexes present in exclusive ring 2-colocalization was slightly smaller than that of postsynaptic complexes within ring 3-colocalization (Fig. 3D). The data for tether–pre AP2q–post AP2a and tether–pre AP2q–post AP2n ring 3-colocalizations were very similar, except for slight shifts toward larger displacements (fig. S10C).

Therefore, our data show that multiple forms of binary interactions exist between tethers and presynaptic and between presynaptic and postsynaptic complexes. Furthermore, binary interactions within subcolumns are characterized by a lateral displacement between complexes (10 to 15 nm), as opposed to the well-aligned (0- to 5-nm) subcolumn-independent interactions. In addition, our data argue that the lateral positioning of tethers in the binary interaction with presynaptic complexes is strongly limiting the formation of subcolumns. This is consistent with a model where lateral and well-aligned interactions involve different proteins, but it leaves the possibility that formation of well-aligned tripartite trans-synaptic binding induces lateral shifts between its components (fig. S10E).

Structural trans-synaptic columns

Last, we proceeded to investigate whether trans-synaptic columns form larger assemblies. On average, there were 0.74 tether centroid, 1.36 presynaptic complexes, and 1.50 postsynaptic complexes per subcolumn. This shows that subcolumns may share components and contain multiple pre- and postsynaptic complexes, raising the possibility that subcolumns form extended structures.

Using univariate Ripley's L function to analyze lateral spatial organization of individual particle sets (*28*, *57*), we found that pre AP2 and post AP2 particles did not cluster significantly (Fig. 4A). Unexpectedly, post AP2a and AP2n particles also did not cluster. As expected, tethers showed significant clustering at length scales of 5 to 15 nm, while tether centroids did not show significant clustering.

However, taking into account only the particles located within subcolumns, both pre and post AP2 particles significantly clustered at length scales of 30 to 50 nm and 15 to 50 nm, respectively (Fig. 4B). Because clustering was detected at length scales larger than the 15-nm scale used to define subcolumns, we conclude that subcolumns are organized in clusters at length scales up to at least 50 nm. Judged by the high variability and the additional maximum of the post AP2 trace at around 100 nm, it is likely that the clustering range was much wider at some synapses. Therefore, we defined structural trans-synaptic columns as clusters of partially overlapping subcolumns (Fig. 4C).

The mean number of structural columns per synapse was 3.6 ± 3.4 (mean ± SD, N = 14 synapses). On average, 2.5 ± 3.0 (mean ± SD) subcolumns formed one column, with a subcolumn area overlap of 19 ± 18% (mean ± SD). Both the number of subcolumns and the number of columns correlated with the number of SVs (Kendall τ test, P = 0.006 and 0.0013, respectively) (Fig. 4D). The values for the stimulated and the phorbol-12,13-dibutyrate (PDBu)–treated synapses were overall consistent with those for the unstimulated, thus justifying pooling all of them together. The area covered by columns per synapse was 6191 ± 5632 nm^2 (mean ± SD, three synapses containing no subcolumns excluded) or 17 ± 12% (mean ± SD) of the total active zone area. This compares with the nanocolumn size of 80 nm (corresponds to a circle of area 5027 nm^2) and fits within the size range of other reported nanodomains (2000 to 50,000 nm^2) (*5*, *6*, *9*). Overall, this variability shows that structural columns are not uniform and may point to a dynamic nature of their formation.

DISCUSSION

Synaptic transmission requires a precise coordination of pre- and postsynaptic complexes. Here, we detected, visualized, and analyzed at a single-nanometer scale tripartite trans-synaptic assemblies comprising tethers, presynaptic and postsynaptic complexes that link SVs, and postsynaptic receptors.

Several findings argue that these subcolumns constitute a structural framework underlying synaptic nanocolumns previously observed by superresolution fluorescence microscopy (*4*). (i) Subcolumns provide a structural link between SVs and iGluRs, thus providing a mechanism for nanocolumn formation (*12*). (ii) Subcolumns contain tethers and iGluRs, which is consistent with nanocolumns because RIM (Rab3-interacting molecule) and AMPAR subunits colocalize in nanocolumns and RIM1α is involved in tether formation (*34*). (iii) Subcolumns are smaller in size than nanocolumns (diameter, 30 versus 80 nm). (iv) Subcolumns cluster and share their components to form larger structures similar in size with nanocolumns.

The detection of assemblies comprising tethers and proteins present in the synaptic cleft supports the model whereby colocalization between neurotransmitter release and reception is mediated by intermediate complexes rather than by neurotransmitter diffusion. On the basis of the radii of SVs and subcolumns, we estimate that subcolumns limit the maximal distance between release sites and receptors to 40 to 50 nm. Because that is still within the estimated area of maximally activated AMPARs (0.01 μm^2 or a circle of 54 nm diameter) (*12*), we conclude that the formation of subcolumns enables a strong synaptic response.

The characteristic lateral displacements of components constituting subcolumns argue that subcolumn formation requires a synergistic binding of tethers and pre- and postsynaptic complexes, and suggest that indirect or bindings mediated by a diffusible protein (*58*) may be involved. In addition, considering that more than the minimally required three complexes are often present within a single subcolumn and that in some cases nearby subcolumns share their constituents, multiple weak or transient interactions may contribute to the formation of structural columns.

To address the difficulties in studying synaptic complexes, which arise from their complexity and low abundance (*2*), we followed an approach that strikes a balance between deciphering larger molecular assemblies and maximizing the resolution of individual complexes. The methods chosen allowed us to simultaneously visualize a multitude

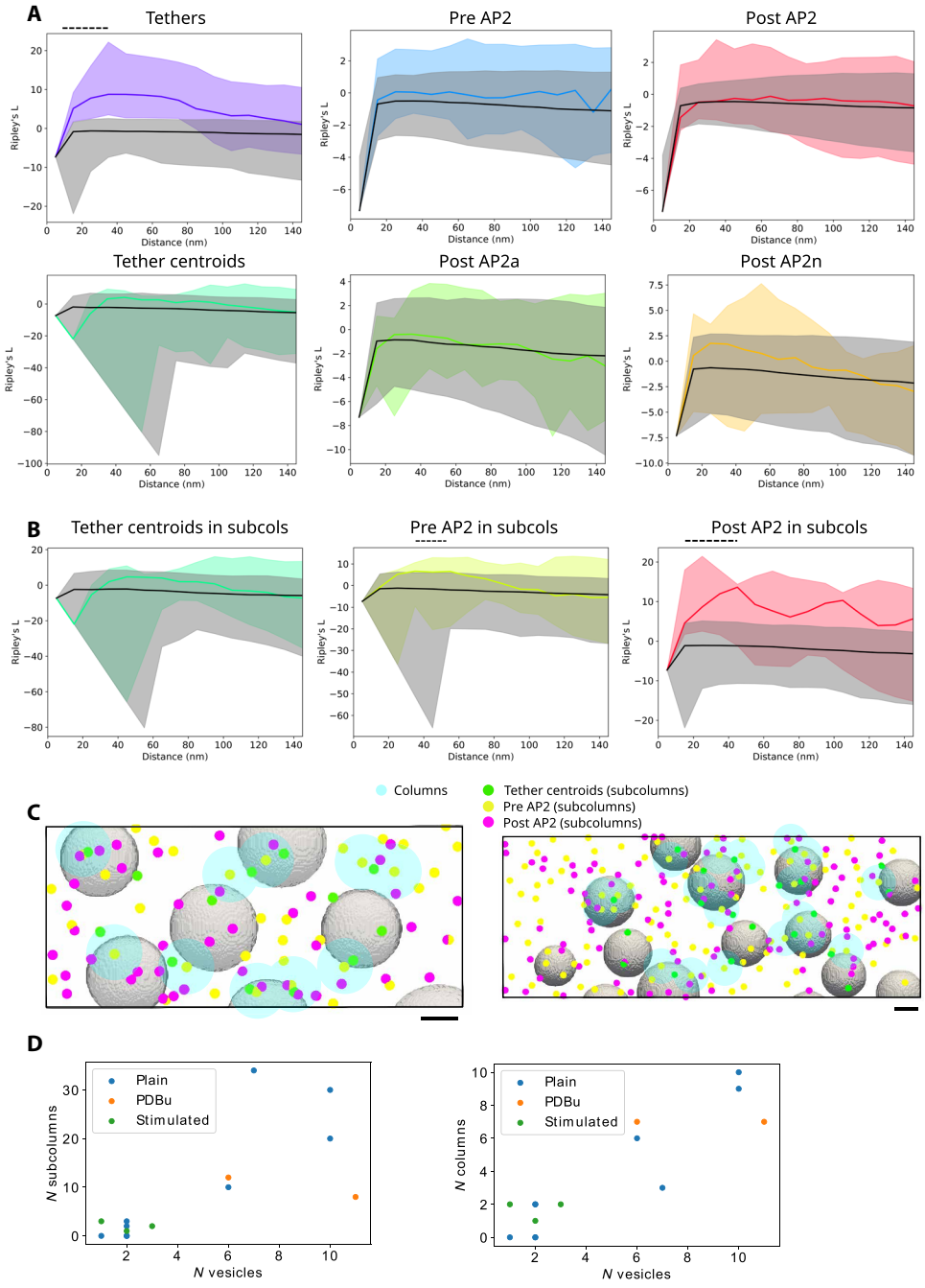

Fig. 4. Structural trans-synaptic columns. (**A**) Univariate clustering of particles, as indicated above the graphs. (**B**) Univariate clustering of particles within subcolumns, as indicated above the graphs. (A and B) Dashed black lines indicate the clustering length range. Ripley's L function is shown for real complexes (in color) and randomly positioned particles (gray). Solid lines show means, color shaded areas are the variation for individual synapses, and gray shaded areas are the 95% confidence limits. (**C**) Examples of columns (transparent blue) superimposed on mapped particles: tether centroids (green), pre AP2 (yellow), and post AP2 complexes (violet). Scale bar, 20 nm. (**D**) Dependence of the number of subcolumns (left) and columns (right) on the number of (tethered) SVs, shown separately for the stimulated (Glu/Gly/KCl), PDBu-treated, and untreated (plain) synapses.

of synaptic complexes, SVs, and plasma membranes at molecular resolution in their native environment. We observed iGluRs in their physiological composition within an environment containing their native membranes and interacting proteins, which control their functional properties (*15*). Because a substantial conformational variability of iGluRs was reported depending on physiological state, pore-forming, and auxiliary subunit composition (*51*, *59*, *60*), AMPARs and NMDARs in our tomograms are expected to be present in a variety of conformations and with different interacting partners. Therefore, our iGluR averages emphasize physiological relevance, providing complementary information to the previously determined high-resolution structures of reconstituted iGluRs.

Structural diversity of native iGluRs, together with a low number of particles, is certainly a factor that limits the resolution we obtained. Further development of automated acquisition methods that addresses the difficulties in finding structures of interest should increase the number of particles and refine the identification of complexes. Previous visualizations of neurotransmitter receptors by conventional and cryo-ET of dissociated neuronal cultures (*43*, *61*, *62*) and recent advances in thinning vitrified samples (*63*, *64*) raise expectations that imaging synapses of intact neurons by cryo-ET will become routine. A previous structural work also showed the qualitative agreement between synaptosomes and synapses in neuronal cultures and the importance of cryo-preparation for molecular imaging of synapses (*26*, *27*, *42*, *43*), which, in combination with the template-free detection and classification (*28*), is uniquely suited for precise molecular localization and identification in complex systems.

An important reason why we could not detect a difference in the trans-synaptic organization between the pharmacologically treated and untreated synapses is the small number of treated synapses. While we expect that the trans-synaptic assemblies could be affected by the pharmacological manipulations, they were found in both treated and untreated synaptosomes, arguing that the trans-synaptic assemblies represent a major synaptic feature that was neither created nor abolished by the treatments. Similarly, while the stimulation we applied likely affects the receptor conformation, the number of stimulated synapses was too small to process them separately and to affect the average densities at our resolution level, given the high conformational variability expected in unstimulated synapses. Therefore, while pursuing synaptic manipulations constitutes a valid future research direction, the level and type of the manipulations used here are unlikely to have affected our conclusions.

Therefore, the data we present support the hypothesis that synaptic function is carried by precisely organized trans-synaptic units. It complements superresolution findings and provides a framework for further single-nanometer scale explorations of synaptic and other large molecular assemblies that require stable or transient structural interactions between multiple complexes present in different cells or cellular regions to exert their function.

MATERIALS AND METHODS

Synaptosomal preparation

Cerebrocortical synaptosomes were extracted from 6- to 8-week-old male Wistar rats as described previously (*32*, *34*, *65*) in accordance with the procedures accepted by the Max Planck Institute for Biochemistry. Briefly, anesthetized animals were sacrificed, and the cortex was extracted and homogenized in homogenization buffer (HB) [0.32 M sucrose, 20 mM dithiothreitol (DTT), and one tablet of cOmplete mini EDTA-free protease inhibitor cocktail (Roche; 10 ml, pH 7.4)] with up to seven strokes at 700 rpm in a Teflon glass homogenizer. Two of four synaptosomal preparations included 50 mM EDTA in the HB. The homogenate was centrifuged for 2 min at 2000*g*, and the pellet was resuspended in HB and centrifuged for another 2 min at 2000*g*. Supernatants from both centrifugations were combined and centrifuged for 12 min at 9500*g*. The pellet was resuspended in HB and loaded onto a three-step Percoll gradient (3, 10, and 23%, Sigma-Aldrich) in HB without protease inhibitor cocktail. The gradients were spun for 6 min at 25,000*g*, and the material accumulated at the 10/23% interface was recovered and diluted to a final volume of 100 ml in Hepes-buffered medium (HBM) [140 mM NaCl, 5 mM KCl, 5 mM $NaHCO_3$, 1.2 mM Na_2HPO_4, 1 mM $MgCl_2$, 10 mM glucose, and 10 mM Hepes (pH 7.4)]. Percoll was removed by an additional washing step with HBM by centrifugation for 10 min at 22,000*g*, and the pellet was resuspended in HBM and immediately used in the experiments. All steps were performed at 4°C. At no point during this procedure are synaptosomes subjected to hypertonic conditions.

Synaptosomes were diluted to 0.7 mg/ml and incubated for 1 hour at 37°C. During incubation, some synaptosomes (2 of 17) were treated with 300 μM Glu, 300 μM Gly, and 30 μM KCl for 1 min, and some (3 of 17) with 1 μM PDBu for 5 min just before vitrification.

An additional hippocampal synaptosomal preparation was obtained following the same protocol, except that synaptosomes were incubated for 20 min before vitrification, at 37°C with monoclonal anti-GluA2 antibodies (clone 6C4, Invitrogen, catalog no. 32-0300) at 1:30 and 1:100 dilutions, and no pharmacological treatments were used.

Stimulation of synaptosomes and Western blots

Synaptosomes were prepared as stated above. After the last resuspension, protein concentration was determined by Protein-UV (Implen NanoPhotometer) and diluted to 1 or 2 mg/ml. Synaptosomes were incubated in HBM (control) and HBM-Mg^{2+}(stimulated) at 37°C for 1 hour. Synaptosomes were stimulated pharmacologically by incubating them for 1 min with (i) 300 μM glutamate and 300 μM glycine (Glu/Gly) and (ii) 300 μM glutamate, 300 μM glycine, and 30 μM KCl (Glu/ Gly/KCl). For Western blots of synaptosomes, stop solution [5 × 250 mM tris-HCl (pH 6.8), 10% (w/v), SDS 50% (w/v), glycerol 0.02% (w/v), and 50 mM DTT] was added to stimulated and control synaptosomes to stop the reaction and denature proteins. Together, three synaptosomal preparations were used.

For the PSD fraction preparation, both stimulated and control synaptosomes were first treated with EDTA (2 mM final) and ice-cold Triton X-100 solution (0.5% final, details are given below) to stop the reactions. The PSD fraction was prepared, as described previously (*66*). Briefly, synaptosomes were incubated for 15 min in ice-cold 0.5% Triton X-100 solution [0.5% Triton X-100, 0.16 M sucrose, 6 mM tris-HCl (pH 8.1)] and then centrifuged at 32,000*g* for 20 min at 4°C in a 75-Ti rotor (Beckman Coulter) to obtain the one Triton PSD pellet. This pellet was resuspended and mixed with the stop solution (see above).

Samples were boiled for 5 min at 95°C before loading them on a gel. Proteins were separated by denaturing discontinuous polyacrylamide gel electrophoresis. The acrylamide concentration was 7.5 and 4% for the separation and stacking gels, respectively. Between 1 and 40 μg of protein were loaded in each lane, and 1- and 1.5-mm-thick gels were used. The same amount was always loaded in each lane of one gel, the three conditions in triplicates (duplicate in one case), different samples next to each other. Proteins were transferred to 0.2-μm pore size polyvinylidene difluoride (PVDF) membrane by semidry transfer. Before assembling the blotting sandwich, PVDF membranes (Millipore) were activated by soaking them in methanol for ~1 min. Following activation, PVDF membranes were soaked in water for 15 min and then in transfer buffer for 30 min. Membranes were blocked for 1 hour in 5% bovine serum albumin (BSA) in TTBS [20 mM tris (pH 7.4), 150 mM NaCl, and 0.1% Tween 20] and washed afterward with TTBS. Membranes were incubated overnight at 4°C in 1% BSA TTBS containing primary antibodies [1:1000 CaMKIIα monoclonal antibody, clone 6G9, Thermo Fisher Scientific

or 1:500 phospho-CaMKIIα (Thr^{286}) monoclonal antibody, clone 22B1, Thermo Fisher Scientific]. After incubation with the primary antibody, membranes were washed and incubated for 1 hour at room temperature in 1% BSA TTBS containing fluorophore-conjugated secondary antibody [1:500 goat anti-mouse immunoglobulin G (H+L), Highly Cross-Adsorbed Secondary Antibody, and Alexa Fluor Plus 488, Thermo Fisher Scientific]. Membranes were then washed in TTBS and in H_2O, dried, and scanned on Amersham Imager 600 (Cytiva). One or two membranes were obtained and imaged from each synaptosomal preparation. For each band on images, signal was corrected by local background, normalized for each gel separately so that the average value was 100, and statistically analyzed and compared using Student's *t* test.

Mass spectrometry

Sample preparation

Synaptosomal fraction and neocortical homogenate prepared as stated above were used as samples. For reduction and alkylation, proteins were incubated with SDC buffer [1% sodium deoxycholate, 40 mM 2-cloroacetamide (Sigma-Aldrich), 10 mM tris(2-carboxyethyl) phosphine (Pierce, Thermo Fisher Scientific) in 100 mM tris-HCl (pH 8.0)] for 20 min at 37°C. Before digestion, the samples were diluted 1:1 with MS-grade water (VWR). Samples were digested overnight at 37°C by addition of 1 μg of trypsin (Promega). The solution of peptides was then acidified with trifluoroacetic acid (Merck) to a final concentration of 1% and a pH value of <2, followed by purification via SCX stage tips.

LC-MS/MS data acquisition

Purified and desalted peptides were loaded onto a 30-cm column (inner diameter: 75 μm; packed in-house with ReproSil-Pur C18-AQ 1.9-μm beads, Dr. Maisch GmbH) via the autosampler of Easy-nanoLC 1000 (Thermo Fisher Scientific) at 50°C. Using the nanoelectrospray interface, eluting peptides were directly sprayed onto a timsTOF Pro mass spectrometer (Bruker). Peptides were loaded in buffer A [0.1% (v/v) formic acid] at 400 nl/min, and the percentage of buffer B (80% acetonitrile and 0.1% formic acid) was ramped from 5 to 25% over 90 min, followed by a ramp to 35% over 30 min, then 58% over the next 5 min, and 95% over the next 5 min, and maintained at 95% for another 5 min.

Data acquisition on timsTOF Pro was performed using otofControl 6.0. The mass spectrometer was operated in a data-dependent PASEF (parallel accumulation–serial fragmentation) mode with one survey thermal ionization mass spectrometry (TIMS)–MS and 10 PASEF MS/MS scans per acquisition cycle. Analysis was performed in a mass scan range from 100 to 1700 mass/charge ratio (m/z) and an ion mobility range from 1/K0 = 1.6 to 0.6 Vs cm^{-2} using equal ion accumulation and ramp time in the dual TIMS analyzer of 100 ms each at a spectra rate of 9.52 Hz. Suitable precursor ions for MS/MS analysis were isolated in a window of 2 Th for $m/z < 700$ and 3 Th for $m/z > 700$ by rapidly switching the quadrupole position in sync with the elution of precursors from the TIMS device. The collision energy was lowered stepwise as a function of increasing ion mobility, starting from 52 eV for 0 to 19% of the TIMS ramp time, 47 eV from 19 to 38%, 42 eV from 38 to 57%, 37 eV from 57 to 76%, and 32 eV until the end. We made use of the m/z and ion mobility information to exclude singly charged precursor ions with a polygon filter mask and further used "dynamic exclusion" to avoid resequencing of precursors that reached a "target value" of 20,000 a.u. (arbitrary units). The ion mobility dimension was calibrated linearly using three ions from the Agilent electrospray ionization liquid chromatography–MS tuning mix (m/z, 1/K0: 622.0289, 0.9848 Vs cm^{-2}; 922.0097, 1.1895 Vs cm^{-2}; 1221.9906, 1.3820 Vs cm^{2}).

Data analysis

Raw data were processed using the MaxQuant (version 1.6.17.0) computational platform (https://nature.com/articles/nbt.1511) with standard settings applied for ion mobility

(https://ncbi.nlm.nih.gov/pmc/articles/PMC7261821/) data. Shortly, the peak list was searched against the Rat UniProt database (29,942 entries, released on 29 June 2020) and a UPS2 protein database (48 entries) with an allowed precursor mass deviation of 4.5 parts per million (ppm) and an allowed fragment mass deviation of 20 ppm. MaxQuant by default enables individual peptide mass tolerances, which was used in the search. Cysteine carbamidomethylation was set as static modification, and methionine oxidation and N-terminal acetylation as variable modifications. Proteins were quantified across samples using the label-free quantification algorithm in MaxQuant as label-free quantification intensities. The intensity-based absolute quantification (iBAQ) option was enabled for quantification of proteins within a sample (using the $\log_{10}$ fit option in MaxQuant).

Among the detected proteins, we selected more than 100 prominent synaptic proteins for analysis. These were selected on the basis of their importance for this study, as well as following the list of proteins determined in (*36*).

The iBAQ values represent the relative molar abundances of proteins within a sample. Therefore, to obtain the copy number per synapse of the detected proteins, an external normalization parameter is needed. We used the number of Bassoon molecules determined in (*36*) (446) for presynaptic [and few common proteins listed in (*36*) and tables S1 and S2] and the generally accepted number of PSD-95 proteins (300) (*48*).

Cryo–electron tomography

For vitrification, a 3-μl drop of 10-nm colloidal gold (Sigma-Aldrich) was deposited on plasma-cleaned, holey carbon copper EM grids (Quantifoil) and allowed to dry. A 3-μl drop of synaptosomes was placed onto the grid, blotted with filter paper (GE Healthcare), and plunged into liquid ethane.

Tilt series were collected under a low-dose acquisition scheme using SerialEM (*67*) on Titan Krios (FEI) equipped with a field emission gun operated at 300 kV, with a post-column energy filter (Gatan) operated in the zero-loss mode and with a computerized cryostage designed to maintain the specimen temperature <−150°C. Images were recorded on a direct electron detector device (K2 Summit operated in the counting mode). Tilt series were typically recorded from −60° to 60° with a 2° angular increment, in two halves starting from 0°. Pixel sizes were 0.34 and 0.42 nm at the specimen level. Volta phase plate with nominal underfocus of 0.5 to 1 μm (*68*) was used. The total dose was kept <100 e^{-}/Å^{2}. Individual frames were aligned using Motioncor2 (*69*). Tilt series were aligned using gold beads as fiducial markers, and 3D reconstructions were obtained by weighted back projection using Imod (*70*). During reconstruction, the projections were binned once and low pass–filtered at the post-binning Nyquist frequency. Tomograms analyzed here showed higher contrast because of the recent developments of the Volta phase plate for electron microscopes and the direct electron detectors (*68*, *71*).

We selected for further processing 14 tomograms from four synaptosomal preparations that were of sufficient technical and biological quality. Specifically, tomograms were deemed technically acceptable

if they did not contain any signs of ice crystal formation such as ice reflections or faceted membranes, and they had reasonable signal-to-noise ratio and proper tomographic alignment. Synaptosomes that showed prominent PSD indicative of the glutamatergic synapses were selected. We discarded synapses showing signs of deterioration such as elliptical small vesicles, strong endocytotic features, broken membranes, or the cleft narrower than 14 nm. Because upon visual inspection there were no obvious differences between the pharmacologically treated (by PDBu and Glu/Gly/KCl) and nontreated synaptosomes, the data were pooled together. In addition, synaptosomes from preparations that included EDTA and those where EDTA was omitted in the HB were among those selected by biological and technical criteria, indicating that they were healthy. Those that contained EDTA in the HB were smaller in size; however, both groups were within the size range that we commonly observe in our synaptosomes.

From the additional synaptosomal preparation, 13 tomograms were recorded and reconstructed in the same way as above, except that the pixel size at the specimen level was 0.439 nm.

Density tracing

The complete image processing workflow is schematically presented in fig. S1.

Synaptic membranes and proximal SVs were segmented using an automated software approach (*72*) or manually by Amira software (Thermo Fisher Scientific). Density tracing, particle picking, and general classification were performed following the procedure described before (*28*). Specifically, tomograms were smoothed by Gaussian low-pass filtering at $\sigma = 1.5$ pixels, and density was traced in 3D using a discrete Morse theory–based software package DisPerSe (*44*) and simplified by the topological persistence. The persistence threshold was set so that for all synapses the density of vertices on the synaptic membranes was 0.006 vertices/nm^3 and the number of arcs was two times higher than the number of vertices. We used the same procedure to trace density on perisynaptic regions of postsynaptic membranes that were not in contact with the PSD from three of the largest synapses. Three of the largest and the best quality tomograms were used.

The Morse density tracing ensures that the vertices are located at the points of grayscale value minima (that is, density maxima) and that each arc propagates along the maximum grayscale gradient and contains a saddle point (having minima in two dimensions and a maximum in the third dimension) (*44*). The simplification by topological persistence reduces the influence of noise by removing spurious minima–saddle point pairs. This way, the vertices represent strong densities and the arcs represent the connecting structures between them. A path is composed of a chain of vertices and arcs, thus connecting more distant vertices.

Detection of complexes (particle picking)

Extracellular pre- and postsynaptic as well as perisynaptic particles were detected from the Morse tracing results by selecting extracellular vertices that satisfy the following geometrical constraints: 8- to 20-nm Euclidean distance to the membrane, 20- to 40-nm geodesic distance (along a path) to the closest membrane vertex, and sinuosity of the path 0 to 3 nm. The projection of selected vertices on the interface between the plasma membrane and the extracellular space was chosen as the particle center. Tethers were defined as arcs linking the SV and the presynaptic membrane vertices that had a geodesic length up to 40 nm. Exclusion (minimal interparticle) distance of 0.5 nm was imposed. Subvolumes of 64 pixels in size at a pixel size of 0.684 nm, centered on the particle locations, were extracted for further processing, yielding 3670 extracellular presynaptic and 5688 extracellular postsynaptic particles. Only the tethered SVs were considered for the colocalization analysis.

Classification by the AP

For each particle, we determined the direction of the vector normal to the membrane at the exact particle position. The direction of the particle normal vectors was initially determined by calculating the direction perpendicular to the membrane at the previously determined particle positions (movie S1). We then improved the precision of the particle positions and normal vectors, by performing one round of high symmetry (C10) constrained refinement (see below). This precise determination of particle positions and normal vectors turned out to be essential for further processing.

AP classifications of pre- and postsynaptic particles followed the same procedure. Particles were rotationally averaged by computing mean grayscale values of two pixel-wide rings around the particle normal vectors and the resulting rotational averages were normalized to a density mean of 0 and SD of 1. Clustering distance between two particles was defined as the cross-correlation coefficient between their rotational averages around vectors normal to the plasma membrane. The AP input preference parameter was −6. For the first round of AP classification, a cylindrical mask was used that included both membrane and extracellular regions (fig. S3, A and C). Classes that did not show clear membrane-bound densities were discarded, leaving 8 of 10, and 17 of 21 pre- and postsynaptic classes, containing 1524 presynaptic (particle set pre AP1) and 2235 postsynaptic particles (post AP1 particle set). The second AP classification yielded 18 presynaptic and 30 postsynaptic classes. The mask was cylindrical, containing only extracellular space (fig. S3, B and D). Class averages obtained from rotationally averaged particles, together with de novo 3D refined class averages, were visually inspected to select AP classes containing well-defined extracellular density, resulting in 12 presynaptic and 18 postsynaptic classes (pre AP2 and post AP2 particle sets, respectively). On the basis of their similarity, these were joined to form four presynaptic and four postsynaptic classes, containing 200 to 600 particles per class (pre AP2p-s and post AP2a, AP2b, AP2c, and AP2n particle sets) for a total of 1074 and 1100 pre- and postsynaptic particles. In this way, pre and post AP1 sets are the most comprehensive, the AP2 sets are the most representative of the full complement of extracellular complexes, while pre AP2p-s and post AP2a, AP2b,AP2 c, and AP2n sets contain distinct classes of complexes. Exclusion distance of 5 nm (for colocalization) or 10 nm (for averaging) was imposed on each particle set before further processing.

Perisynaptic particles were classified in the same way, except that all AP1 classes (seven in total, 3765 particles) were retained and further processed, although these classes would have been removed if the criteria used for synaptic classes were applied. The second AP classification yielded 21 classes. Average 3D densities of the individual AP2 classes were determined by external reference-free (de novo), constrained 3D refinement (see below).

Structure determination by subtomogram averaging

3D classification and refinement steps were performed in Relion (*73*). During the refinement, particle half-datasets were processed

independently according to the "gold standard" procedure, as implemented in Relion. Unless stated explicitly, all refinements were performed de novo, that is, without the use of external references. For de novo processing, initial references were obtained by aligning all particles according to the two angles determined from normals and randomizing the third angle (around the normal direction) to remove the missing wedge. The structures shown were automatically filtered at the gold standard resolution determined by Relion. No symmetry was used unless noted otherwise.

For the constrained refinement and 3D classification, particle alignment was optimized by allowing only small changes of angles corresponding to the direction of the normal vector and small spatial displacements. The alignment around the third angle (around the normal vector) was optimized over the entire angular range, except when a high symmetry was used (C10). To implement this, we set the prior values for angles *tilt* and *psi* in Relion particle star files to the two angles defining the normals to the membrane and specified small values (3.66) for the SDs of these two angles in the refine command options. In case of the constrained refinement of AP2 class averages, particles were randomly rotated around membrane normals to remove any possible bias arising from a previous assignment of the angle around the normals.

De novo post AP2a average contained 566 particles, and post AP2n contained 532 particles. In both cases, 10-nm exclusion distance was imposed to avoid double picking. De novo 3D refinements of iGluRs were performed independently on post AP2a and post AP2n sets. De novo 3D class averages were obtained from 317 (AMPAR) and 177 NMDAR particles. We also obtained de novo 3D class averages with C2 symmetry because it is commonly used for high-resolution structures of AMPARs and NMDARs. Initial model–based 3D classification and averaging used PDB-6QKZ (AMPAR) and PDB-6MMB (NMDAR) atomic models. These models were Gaussian low pass–filtered to 6 nm. The initial model–based 3D class averages contained 257 (AMPAR) and 120 (NMDAR) particles. The resolution values determined by Fourier shell correlation at the FSC = 0.143 criterion are 33, 31, 31, and 34 Å for AP2a derived de novo, de novo 3D class, de novo 3D class C2, and initial model based, respectively, and 34, 36, 29, and 34 Å for AP2n derived de novo, de novo 3D class, de novo 3D class C2, and initial model based, respectively.

To obtain a robust estimate of the receptor height in fig. S4B, density traces show the 10th highest grayscale value on each z-slice. Essentially the same results were obtained for the whole range between the 1st and 100th grayscale value.

An independent postsynaptic particle set was obtained from the additional tomograms (see above) following the same density tracing, complex detection, and AP classification procedures as explained above, resulting in classes corresponding to AP2a (594 particles) and AP2n (205 particles). Subtomogram averaging was also performed in the same way but independently from the main particle set. The averages were automatically filtered at the resolution determined (30 to 41 Å for averages determined from AP2a-like and 34 to 45 Å from AP2n-like particles) by Relion software. Because by visual assessment of the averages these resolution estimates appeared to overestimate the resolution, the averages were slightly smoothed by Gaussian filtering (σ = 8.4 Å). Average densities obtained from the independent particle set are shown in fig. S8. The independently obtained particle sets could not be mixed with (the main) AP2a and AP2n sets, because they had different pixel sizes.

Trans-synaptic colocalization

The 2-colocalization between particle sets located on different synaptic layers (presynaptic cytosolic, extracellular presynaptic, and extracellular postsynaptic) at a given colocalization distance is defined as the number of particles from the first set that has at least one particle from the other set within their colocalization neighborhoods. The colocalization (or trans-synaptic) neighborhood of a particle is defined as the cylinder centered at the particle, its axis perpendicular to the presynaptic membrane, and its base radius equal to the colocalization distance (see the schemes in fig. S9). The colocalizations were implemented by projecting all particles on the intracellular interface of the presynaptic membrane and calculating the 3D Euclidean distance between projected particles originating at different layers. The distance calculated in this way represents only the lateral (cis-synaptic) distance between particles; the distance in the trans-synaptic direction is irrelevant. All colocalizations were calculated for colocalization distances of 5, 10, …, 35 nm.

Colocalizations between three different particle sets (3-colocalizations) were defined in the same way, except that at least one particle from each of the three different particle sets has to belong to the colocalization neighborhood (see the schemes on Fig. 3A).

Ring colocalizations were defined in the same way as the 2- and 3-colocalizations (above), except that the colocalization neighborhood takes the form of concentric cylindrical trans-synaptic rings, for both 2- and 3-colocalizations (see schemes in Fig. 3D and fig. S10C). These were calculated by subtracting colocalization numbers between consecutive distances.

Exclusive 2-colocalizations were defined as those 2-colocalizations that are not present in the 3-colocalizations, at the same colocalization distance. The number of particles in exclusive 2-colocalizations is obtained by subtracting the number of particles in the corresponding 3-colocalizations from the 2-colocalizations. In this work, we used only exclusive ring 2-colocalizations. We note that these may be negative, as a result of a particular localization of particles within 3-colocalizations. For example, given particle sets A, B, and C, if particles from sets A and B colocalize at a 5-nm distance, the number of exclusive 2-colocalizations at 0 to 5 nm is 1. Furthermore, if a particle from set C colocalizes with the other two only at 10 nm, the number of exclusive 2-colocalizations at 5- to 10-nm ring is obtained as the number of 2-colocalization at 5- to 10-nm ring (0) minus the number of 3-colocalizations at 5- to 10-nm ring (1), that is, −1.

In some cases, the data were presented as the number of colocalizations at a given colocalization distance divided by the corresponding colocalization area (area of a circle of radius equal to the colocalization distance) (fig. S9B) or divided by the area of colocalization rings (Fig. 3D and fig. S10C).

Colocalization analysis involved pre and post AP1 and AP2 particle sets, AP2 classes, tethers, and tethered SVs (65 in total). We used centroids obtained by spatially clustering tethers to represent tethers (137 in total), to remove the influence of clustering of tethers induced by SVs on the colocalization results. Additional benefit of this approach was that the number of tether centroids was comparable to the number of SVs, which facilitated comparison between the corresponding colocalizations. The position of an SV was defined as the position of its closest pixel to the presynaptic membrane. For each 3-colocalization, the number of particles within the cylinders was calculated. To avoid double picking, the exclusion distance of 5 nm was imposed on each set separately.

Statistical significance of 3-colocalizations was determined by Monte Carlo random simulations. To avoid bias arising from a possible nonrandom distribution or real particle sets, random simulation models were created so that one particle set was kept fixed at the real particle locations and the other one (for 2-colocalizations) or the other two (for 3-colocalizations) simulated particle sets were generated by randomly distributing the same number of particles (as in the real sets) on the same synaptic geometry (*57*). Each time, 200 random simulation cases were generated and the number of colocalizations was determined. This procedure was repeated twice for each 2-colocalization and three times for 3-colocalizations, and each particle set was kept at the real locations once, resulting in 400 random simulations for each 2-colocalization and 600 random simulations for each 3-colocalization. The fraction of all simulation results that yielded a lower or equal number of 3-colocalization events compared to the real 3-colocalization number represents the probability that the real colocalization is different from the random model. This probability is denoted (and shown on graphs) as $1 - P$ value, where the P value is then the probability that the null hypothesis is correct.

Trans-synaptic subcolumns were defined as 3-colocalization events between tether centroids, pre AP2, and post AP2 particles at 15-nm colocalization distance. Structurally defined trans-synaptic columns were obtained by a simple union of partially overlapping subcolumns. This method can be regarded as a parameter-free version of density-based spatial clustering of applications with noise, where the minimum number of points is 1 and the neighborhood radius is simply the distance that defines subcolumns.

Univariate particle distribution analysis

Univariate clustering of a given particle set was determined by Ripley's L function, using Euclidean distance between particles, as explained before (*28*, *57*, *74*). This function is often used for the analysis of spatial point patterns at multiple length scales because it considers the distribution of distances from a particle to multiple neighbors, thus providing a more comprehensive clustering information than the nearest neighbor and other first-order functions (*28*, *57*). Statistical significance of particle clustering was determined by Monte Carlo random simulations, where the same number of particles was randomly distributed on the same synaptic geometry. Ripley's L was calculated for 200 simulations, and the envelope within which 95% of the curves were located was then used to determine whether the distribution of the particle set was significantly different from the random distribution (at the $P < 0.05$ significance level). A clustering is said to be significant at the range of length scales that starts at the lowest scale where Ripley's L is significant and ends at the scale where Ripley's L reaches a maximum (but is still above the 95% significance), as customary in the field (*75*). For clustering of subcolumns, the clustering range can start only at 15 nm because subcolumns are created by imposing a 15-nm distance (Fig. 4C).

Statistical analysis

Statistical significance for colocalizations and univariate Ripley's L function was calculated using Monte Carlo random simulations, as explained above. Student's t test was used for the Western blot analysis. Kendall τ test (nonparametric) was used for testing correlation between number of SVs and numbers of subcolumns and columns.

Software methods

Particle picking, AP classification, spatial clustering, and colocalization analysis were performed in Python using PySeg package (*28*). PySeg depends on Pyto (*76*), Numpy VTK (*77*), and *matplotlib* library (*78*). For visualization, Paraview (*79*) and the University of California San Francisco Chimera package (*80*) software packages were used. All computations were done on Linux clusters at the computer center of the Max Planck Institute of Biochemistry.

The complete software, together with all dependencies, is installed as PySeg capsule on Code Ocean (PySeg). The latest version of the software is available on GitHub (PySeg) and upon demand.

SUPPLEMENTARY MATERIALS

Supplementary material for this article is available at http://advances.sciencemag.org/cgi/content/full/7/10/eabe6204/DC1

REFERENCES AND NOTES

1. B. Alberts, The cell as a collection of protein machines: Preparing the next generation of molecular biologists. *Cell* **92**, 291–294 (1998).
2. R. A. W. Frank, N. H. Komiyama, T. J. Ryan, F. Zhu, T. J. O'Dell, S. G. N. Grant, Nmda receptors are selectively partitioned into complexes and supercomplexes during synapse maturation. *Nat. Commun.* **7**, 11264 (2016).
3. K. Perez de Arce, N. Schrod, S. W. R. Metzbower, E. Allgeyer, G. K.-W. Kong, A.-H. Tang, A. J. Krupp, V. Stein, X. Liu, J. Bewersdorf, T. A. Blanpied, V. Lucic, T. Biederer, Topographic mapping of the synaptic cleft into adhesive nanodomains. *Neuron* **88**, 1165–1172 (2015).
4. A.-H. Tang, H. Chen, T. P. Li, S. R. Metzbower, H. D. MacGillavry, T. A. Blanpied, A trans-synaptic nanocolumn aligns neurotransmitter release to receptors. *Nature* **536**, 210–214 (2016).
5. H. D. MacGillavry, Y. Song, S. Raghavachari, T. A. Blanpied, Nanoscale scaffolding domains within the postsynaptic density concentrate synaptic ampa receptors. *Neuron* **78**, 615–622 (2013).
6. D. Nair, E. Hosy, J. D. Petersen, A. Constals, G. Giannone, D. Choquet, J. B. Sibarita, Super-resolution imaging reveals that AMPA receptors inside synapses are dynamically organized in nanodomains regulated by PSD95. *J. Neurosci.* **33**, 13204–13224 (2013).
7. I. Chamma, M. Letellier, C. Butler, B. Tessier, K.-H. Lim, I. Gauthereau, D. Choquet, J.-B. Sibarita, S. Park, M. Sainlos, O. Thoumine, Mapping the dynamics and nanoscale organization of synaptic adhesion proteins using monomeric streptavidin. *Nat. Commun.* **7**, 10773 (2016).
8. D. Maschi, V. A. Klyachko, Spatiotemporal regulation of synaptic vesicle fusion sites in central synapses. *Neuron* **94**, 65–73.e3 (2017).
9. M. Hruska, N. Henderson, S. J. Le Marchand, H. Jafri, M. B. Dalva, Synaptic nanomodules underlie the organization and plasticity of spine synapses. *Nat. Neurosci.* **21**, 671–682 (2018).
10. O. O. Glebov, R. E. Jackson, C. M. Winterflood, D. M. Owen, E. A. Barker, P. Doherty, H. Ewers, J. Burrone, Nanoscale structural plasticity of the active zone matrix modulates presynaptic function. *Cell Rep.* **18**, 2715–2728 (2017).
11. A. C. Penn, C. L. Zhang, F. Georges, L. Royer, C. Breillat, E. Hosy, J. D. Petersen, Y. Humeau, D. Choquet, Hippocampal ltp and contextual learning require surface diffusion of ampa receptors. *Nature* **549**, 384–388 (2017).
12. T. Biederer, P. S. Kaeser, T. A. Blanpied, Transcellular nanoalignment of synaptic function. *Neuron* **96**, 680–696 (2017).
13. S. F. Traynelis, L. P. Wollmuth, C. J. McBain, F. S. Menniti, K. M. Vance, K. K. Ogden, K. B. Hansen, H. Yuan, S. J. Myers, R. Dingledine, Glutamate receptor ion channels: Structure, regulation, and function. *Pharmacol. Rev.* **62**, 405–496 (2010).
14. R. A. Nicoll, A brief history of long-term potentiation. *Neuron* **93**, 281–290 (2017).
15. J. Schwenk, N. Harmel, A. Brechet, G. Zolles, H. Berkefeld, C. S. Müller, W. Bildl, D. Baehrens, B. Hüber, A. Kulik, N. Klöcker, U. Schulte, B. Fakler, High-resolution proteomics unravel architecture and molecular diversity of native ampa receptor complexes. *Neuron* **74**, 621–633 (2012).
16. B. Herguedas, J. F. Watson, H. Ho, O. Cais, J. García-Nafría, I. H. Greger, Architecture of the heteromeric glua1/2 ampa receptor in complex with the auxiliary subunit tarp γ8. *Science* **364**, eaav9011 (2019).
17. T. Nakagawa, Structures of the AMPA receptor in complex with its auxiliary subunit cornichon. *Science* **366**, 1259–1263 (2019).
18. F. Jalali-Yazdi, S. Chowdhury, C. Yoshioka, E. Gouaux, Mechanisms for zinc and proton inhibition of the GluN1/GluN2A NMDA receptor. *Cell* **175**, 1520–1532.e15 (2018).
19. E. C. Twomey, M. V. Yelshanskaya, R. A. Grassucci, J. Frank, A. I. Sobolevsky, Channel opening and gating mechanism in AMPA-subtype glutamate receptors. *Nature* **549**, 60–65 (2017).

20. Y. Zhao, S. Chen, A. C. Swensen, W.-J. Qian, E. Gouaux, Architecture and subunit arrangement of native AMPA receptors elucidated by cryo-EM. *Science* **364**, 355–362 (2019).
21. V. Lučič, A. Rigort, W. Baumeister, Cryo-electron tomography: The challenge of doing structural biology in situ. *J. Cell Biol.* **202**, 407–419 (2013).
22. K. A. Taylor, R. M. Glaeser, Electron diffraction of frozen, hydrated protein crystals. *Science* **186**, 1036–1037 (1974).
23. J. Dubochet, M. Adrian, J. J. Chang, J. C. Homo, J. Lepault, A. W. McDowall, P. Schultz, Cryo-electron microscopy of vitrified specimens. *Q. Rev. Biophys.* **21**, 129–228 (1988).
24. J. Dubochet, N. Sartori Blanc, The cell in absence of aggregation artifacts. *Micron* **32**, 91–99 (2001).
25. C. K. E. Bleck, A. Merz, M. G. Gutierrez, P. Walther, J. Dubochet, B. Zuber, G. Griffiths, Comparison of different methods for thin section EM analysis of *Mycobacterium smegmatis*. *J. Microsc.* **237**, 23–38 (2010).
26. B. Zuber, V. Lučić, Molecular architecture of the presynaptic terminal. *Curr. Opin. Struct. Biol.* **54**, 129–138 (2019).
27. Y.-T. Liu, C.-L. Tao, P.-M. Lau, Z. H. Zhou, G.-Q. Bi, Postsynaptic protein organization revealed by electron microscopy. *Curr. Opin. Struct. Biol.* **54**, 152–160 (2019).
28. A. Martinez-Sanchez, Z. Kochovski, U. Laugks, J. M. z. A. Borgloh, S. Chakraborty, S. Pfeffer, W. Baumeister, V. Lučić, Template-free detection and classification of membrane-bound complexes in cryo-electron tomograms. *Nat. Methods* **17**, 209–216 (2020).
29. V. P. Whittaker, Thirty years of synaptosome research. *J. Neurocytol.* **22**, 735–742 (1993).
30. P. R. Dunkley, P. E. Jarvie, P. J. Robinson, A rapid percoll gradient procedure for preparation of synaptosomes. *Nat. Protoc.* **3**, 1718–1728 (2008).
31. D. G. Nicholls, T. S. Sihra, Synaptosomes possess an exocytotic pool of glutamate. *Nature* **321**, 772–773 (1986).
32. M. D. C. Godino, M. Torres, J. Sánchez-Prieto, Cb1 receptors diminish both ca^{2+} influx and glutamate release through two different mechanisms active in distinct populations of cerebrocortical nerve terminals. *J. Neurochem.* **101**, 1471–1482 (2007).
33. R. Fernández-Busnadiego, B. Zuber, U. E. Maurer, M. Cyrklaff, W. Baumeister, V. Lucic, Quantitative analysis of the native presynaptic cytomatrix by cryoelectron tomography. *J. Cell Biol.* **188**, 145–156 (2010).
34. R. Fernández-Busnadiego, S. Asano, A. Oprişoreanu, E. Sakata, M. Doengi, Z. Kochovski, M. Zürner, V. Stein, S. Schoch, W. Baumeister, V. Lučić, Cryo-electron tomography reveals a critical role of rim1α in synaptic vesicle tethering. *J. Cell Biol.* **201**, 725–740 (2013).
35. K. Shen, T. Meyer, Dynamic control of CAMKII translocation and localization in hippocampal neurons by NMDA receptor stimulation. *Science* **284**, 162–166 (1999).
36. B. G. Wilhelm, S. Mandad, S. Truckenbrodt, K. Kröhnert, C. Schäfer, B. Rammner, S. J. Koo, G. A. Claßen, M. Krauss, V. Haucke, H. Urlaub, S. O. Rizzoli, Composition of isolated synaptic boutons reveals the amounts of vesicle trafficking proteins. *Science* **344**, 1023–1028 (2014).
37. Y. Sugiyama, I. Kawabata, K. Sobue, S. Okabe, Determination of absolute protein numbers in single synapses by a GFP-based calibration technique. *Nat. Methods* **2**, 677–684 (2005).
38. X. Chen, L. Vinade, R. D. Leapman, J. D. Petersen, T. Nakagawa, T. M. Phillips, M. Sheng, T. S. Reese, Mass of the postsynaptic density and enumeration of three key molecules. *Proc. Natl. Acad. Sci. U.S.A.* **102**, 11551–11556 (2005).
39. D. Cheng, C. C. Hoogenraad, J. Rush, E. Ramm, M. A. Schlager, D. M. Duong, P. Xu, S. R. Wijayawardana, J. Hanfelt, T. Nakagawa, M. Sheng, J. Peng, Relative and absolute quantification of postsynaptic density proteome isolated from rat forebrain and cerebellum. *Mol. Cell. Proteomics* **5**, 1158–1170 (2006).
40. B. Zuber, I. Nikonenko, P. Klauser, D. Muller, J. Dubochet, The mammalian central nervous synaptic cleft contains a high density of periodically organized complexes. *Proc. Natl. Acad. Sci. U.S.A.* **102**, 19192–19197 (2005).
41. V. Lučić, A. H. Kossel, T. Yang, T. Bonhoeffer, W. Baumeister, A. Sartori, Multiscale imaging of neurons grown in culture: From light microscopy to cryo-electron tomography. *J. Struct. Biol.* **160**, 146–156 (2007).
42. N. Schrod, D. Vanhecke, U. Laugks, V. Stein, Y. Fukuda, M. Schaffer, W. Baumeister, V. Lucic, Pleomorphic linkers as ubiquitous structural organizers of vesicles in axons. *PLOS ONE* **13**, e0197886 (2018).
43. C.-L. Tao, Y.-T. Liu, R. Sun, B. Zhang, L. Qi, S. Shivakoti, C.-L. Tian, P. Zhang, P.-M. Lau, Z. H. Zhou, G.-Q. Bi, Differentiation and characterization of excitatory and inhibitory synapses by cryo-electron tomography and correlative microscopy. *J. Neurosci.* **38**, 1493–1510 (2018).
44. T. Sousbie, The persistent cosmic web and its filamentary structure—I. Theory and implementation. *Mon. Notices Royal Astron. Soc.* **414**, 350–383 (2011).
45. B. J. Frey, D. Dueck, Clustering by passing messages between data points. *Science* **315**, 972–976 (2007).
46. A. Yamagata, S. Fukai, Structural insights into leucine-rich repeat-containing synaptic cleft molecules. *Curr. Opin. Struct. Biol.* **54**, 68–77 (2019).
47. H. Liu, Synaptic organizers: Synaptic adhesion-like molecules (SALMs). *Curr. Opin. Struct. Biol.* **54**, 59–67 (2019).
48. M. Sheng, C. C. Hoogenraad, The postsynaptic architecture of excitatory synapses: A more quantitative view. *Annu. Rev. Biochem.* **76**, 823–847 (2007).
49. F. Jaskolski, F. Coussen, C. Mulle, Subcellular localization and trafficking of kainate receptors. *Trends Pharmacol. Sci.* **26**, 20–26 (2005).
50. A. P. Burada, R. Vinnakota, J. Kumar, Cryo-EM structures of the ionotropic glutamate receptor GluD1 reveal a non-swapped architecture. *Nat. Struct. Mol. Biol.* **27**, 84–91 (2020).
51. J. X. Wang, H. Furukawa, Dissecting diverse functions of NMDA receptors by structural biology. *Curr. Opin. Struct. Biol.* **54**, 34–42 (2019).
52. E. Jacobi, J. von Engelhardt, Diversity in AMPA receptor complexes in the brain. *Curr. Opin. Neurobiol.* **45**, 32–38 (2017).
53. J. F. Watson, H. Ho, I. H. Greger, Synaptic transmission and plasticity require AMPA receptor anchoring via its N-terminal domain. *eLife* **6**, e23024 (2017).
54. J. Díaz-Alonso, Y. J. Sun, A. J. Granger, J. M. Levy, S. M. Blankenship, R. A. Nicoll, Subunit-specific role for the amino-terminal domain of AMPA receptors in synaptic targeting. *Proc. Natl. Acad. Sci. U.S.A.* **114**, 7136–7141 (2017).
55. T. Nakagawa, Y. Cheng, E. Ramm, M. Sheng, T. Walz, Structure and different conformational states of native AMPA receptor complexes. *Nature* **433**, 545–549 (2005).
56. I. H. Greger, J. F. Watson, S. G. Cull-Candy, Structural and functional architecture of AMPA-type glutamate receptors and their auxiliary proteins. *Neuron* **94**, 713–730 (2017).
57. T. Wiegand, K. A. Moloney, Rings, circles, and null-models for point pattern analysis in ecology. *Oikos* **104**, 209–229 (2004).
58. K. Matsuda, E. Miura, T. Miyazaki, W. Kakegawa, K. Emi, S. Narumi, Y. Fukazawa, A. Ito-Ishida, T. Kondo, R. Shigemoto, M. Watanabe, M. Yuzaki, Cbln1 is a ligand for an orphan glutamate receptor δ2, a bidirectional synapse organizer. *Science* **328**, 363–368 (2010).
59. S. Chen, E. Gouaux, Structure and mechanism of AMPA receptor–auxiliary protein complexes. *Curr. Opin. Struct. Biol.* **54**, 104–111 (2019).
60. A. Kamalova, T. Nakagawa, AMPA receptor structure and auxiliary subunits. *J. Physiol.* **599**, 453–469 (2020).
61. X. Chen, C. Winters, R. Azzam, X. Li, J. A. Galbraith, R. D. Leapman, T. S. Reese, Organization of the core structure of the postsynaptic density. *Proc. Natl. Acad. Sci. U.S.A.* **105**, 4453–4458 (2008).
62. Y.-T. Liu, C.-L. Tao, X. Zhang, W. Xia, D.-Q. Shi, L. Qi, C. Xu, R. Sun, X.-W. Li, P.-M. Lau, Z. H. Zhou, G.-Q. Bi, Mesophasic organization of $GABA_A$ receptors in hippocampal inhibitory synapses. *Nat. Neurosci.* **23**, 1589–1596 (2020).
63. M. Marko, C. Hsieh, R. Schalek, J. Frank, C. Mannella, Focused-ion-beam thinning of frozen-hydrated biological specimens for cryo-electron microscopy. *Nat. Methods* **4**, 215–217 (2007).
64. M. Schaffer, S. Pfeffer, J. Mahamid, S. Kleindiek, T. Laugks, S. Albert, B. D. Engel, A. Rummel, A. J. Smith, W. Baumeister, J. M. Plitzko, A cryo-FIB lift-out technique enables molecular-resolution cryo-ET within native *Caenorhabditis elegans* tissue. *Nat. Methods* **16**, 757–762 (2019).
65. P. R. Dunkley, J. W. Heath, S. M. Harrison, P. E. Jarvie, P. J. Glenfield, J. A. P. Rostas, A rapid Percoll gradient procedure for isolation of synaptosomes directly from an S_1 fraction: Homogeneity and morphology of subcellular fractions. *Brain Res.* **441**, 59–71 (1988).
66. K. O. Cho, C. A. Hunt, M. B. Kennedy, The rat brain postsynaptic density fraction contains a homolog of the *Drosophila* discs-large tumor suppressor protein. *Neuron* **9**, 929–942 (1992).
67. D. N. Mastronarde, Automated electron microscope tomography using robust prediction of specimen movements. *J. Struct. Biol.* **152**, 36–51 (2005).
68. R. Danev, B. Buijsse, M. Khoshouei, J. M. Plitzko, W. Baumeister, Volta potential phase plate for in-focus phase contrast transmission electron microscopy. *Proc. Natl. Acad. Sci. U.S.A.* **111**, 15635–15640 (2014).
69. S. Q. Zheng, E. Palovcak, J.-P. Armache, K. A. Verba, Y. Cheng, D. A. Agard, Motioncor2: Anisotropic correction of beam-induced motion for improved cryo-electron microscopy. *Nat. Methods* **14**, 331–332 (2017).
70. J. R. Kremer, D. N. Mastronarde, J. R. McIntosh, Computer visualization of three-dimensional image data using IMOD. *J. Struct. Biol.* **116**, 71–76 (1996).
71. G. McMullan, A. Faruqi, R. Henderson, Direct electron detectors. *Methods Enzymol.* **579**, 1–17 (2016).
72. A. Martinez-Sanchez, I. Garcia, S. Asano, V. Lucic, J.-J. Fernandez, Robust membrane detection based on tensor voting for electron tomography. *J. Struct. Biol.* **186**, 49–61 (2014).
73. T. A. M. Bharat, S. H. W. Scheres, Resolving macromolecular structures from electron cryo-tomography data using subtomogram averaging in RELION. *Nat. Protoc.* **11**, 2054–2065 (2016).
74. B. D. Ripley, *Spatial Statistics* (Willey-Interscience, 1981).
75. M. A. Kiskowski, J. F. Hancock, A. K. Kenworthy, On the use of Ripley's K-function and its derivatives to analyze domain size. *Biophys. J.* **97**, 1095–1103 (2009).

76. V. Lučić, R. Fernández-Busnadiego, U. Laugks, W. Baumeister, Hierarchical detection and analysis of macromolecular complexes in cryo-electron tomograms using pyto software. *J. Struct. Biol.* **196**, 503–514 (2016).
77. W. J. Schroeder, B. Lorensen, K. Martin, *The Visualization Toolkit: An Object-Oriented Approach to 3D Graphics* (Kitware, 2004).
78. J. D. Hunter, Matplotlib: A 2D graphics environment. *Comput. Sci. Eng.* **9**, 90–95 (2007).
79. U. Ayachit, *The Paraview Guide: A Parallel Visualization Application* (Kitware, 2015).
80. E. F. Pettersen, T. D. Goddard, C. C. Huang, G. S. Couch, D. M. Greenblatt, E. C. Meng, T. E. Ferrin, UCSF chimera—A visualization system for exploratory research and analysis. *J. Comput. Chem.* **25**, 1605–1612 (2004).

Acknowledgments: We would like to thank F. Beck and F. Meissner for discussions, G. J. Greif and M. Turk for critical reading of the manuscript, and the core facility of the Max Planck Institute of Biochemistry for performing MS measurements. **Funding:** A.M.-S. was the recipient of a postdoctoral fellowship from the Séneca Foundation. This work was supported by DFG LU 1819/2-1 grant, the European Commission under grant FP7 GA ERC-2012-SyG_318987–ToPAG, HFSP RGP0020/2019 grant, and the Max Planck Society. A.M.-S. was supported by the Deutsche Forschungsgemeinschaft (DFG, German Research Foundation) under Germany's Excellence Strategy - EXC 2067/1-390729940. **Author contributions:** A.M.-S. designed and implemented the software. U.L., Z.K., and C.P. acquired tomograms. A.M.-S. and V.L. analyzed the data. L.Z. provided scientific input. W.B. provided resources and acquired funding. V.L. conceived, designed, and supervised the research. V.L. wrote the manuscript. All authors edited the manuscript. **Competing interests:** The authors declare that they have no competing interests. **Data and materials availability:** The following EM densities have been deposited in the EMDataBank: de novo subtomogram averages of complete post AP2a (EMD-11404) and post AP2n (EMD-11405) particle sets, de novo 3D class averages without and with C2 from AP2a (EMD-11406, EMD-11408) and AP2n (EMD-11407, EMD-11409) sets, and 3D class averages obtained using external initial models from AP2a (EMD-11410) and AP2n (EMD-11411) sets.

Submitted 2 September 2020
Accepted 22 January 2021
Published 5 March 2021
10.1126/sciadv.abe6204

Citation: A. Martinez-Sanchez, U. Laugks, Z. Kochovski, C. Papantoniou, L. Zinzula, W. Baumeister, V. Lučić, Trans-synaptic assemblies link synaptic vesicles and neuroreceptors. *Sci. Adv.* **7**, eabe6204 (2021).

ScienceAdvances

Trans-synaptic assemblies link synaptic vesicles and neuroreceptors

Antonio Martinez-SanchezUlrike LaugksZdravko KochovskiChristos PapantoniouLuca ZinzulaWolfgang BaumeisterVladan Lu#i#

Sci. Adv., 7 (10), eabe6204. • DOI: 10.1126/sciadv.abe6204

Science Advances (ISSN 2375-2548) is published by the American Association for the Advancement of Science. 1200 New York Avenue NW, Washington, DC 20005. The title *Science Advances* is a registered trademark of AAAS.